NANO LETTERS

Letter

pubs.acs.org/NanoLett

Correlating Superlattice Polymorphs to Internanoparticle Distance, Packing Density, and Surface Lattice in Assemblies of PbS Nanoparticles

Zhongwu Wang,*[,†] Constanze Schliehe,[∥] Kaifu Bian,[‡] Darren Dale,[†] William A. Bassett,[§] Tobias Hanrath,[‡] Christian Klinke,[⊥] and Horst Weller[⊥]

[†]Cornell High Energy Synchrotron Source, [‡]School of Chemical and Biomolecular Engineering, and [§]Department of Earth and Atmospheric Sciences, Cornell University, Ithaca, New York 14853, United States

[∥]Department of Colloid Chemistry, Max Planck Institute of Colloids and Interfaces, 14476 Potsdam, Germany

[⊥]Institute of Physical Chemistry, University of Hamburg, 20146 Hamburg, Germany

Supporting Information

ABSTRACT: Assemblies of 3.5 nm PbS nanoparticles (NPs) nucleate in three dominant superlattice polymorphs: amorphous, body-centered-cubic (bcc) and face-centered-cubic (fcc) phase. This superlattice relationship can be controlled by the inter-NP distance without changing the NP size. Upon increase of inter-NP distance, the packing density decreases, and the capping molecules at NP surfaces change in structure and accordingly modify the surface energy. The driving force for NP assembly develops from an entropic maximization to a reduction of total free energy through multiple interactions between surface molecules and NPs and resulting variation of surface molecules. Upon long-term aging and additional thermal treatment, fcc undergoes a tetragonal distortion and subsequently transforms to bcc phase, and simultaneously, the NPs embedded in supercrystals reduce surface energy primarily in {200} facets. Linking molecule-NP interactions with a series of changes of packing density and surface lattice spacings of NPs allows for an interpretation of principles governing the nucleation, structure stability, and transformation of PbS NP-assembled supercrystals.

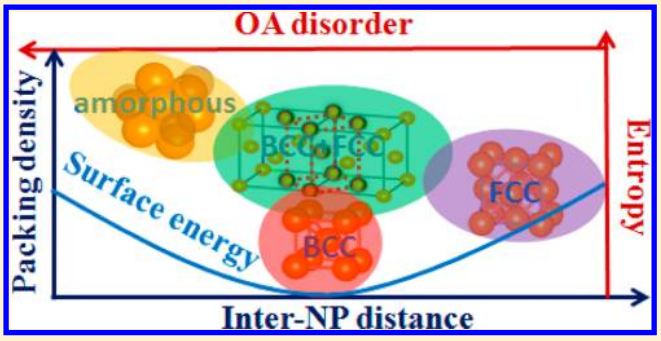

KEYWORDS: *PbS nanoparticle, superlattice, transformation, inter-nanoparticle distance, packing density, surface energy*

The assembly of nanoparticles (NPs) into periodically ordered superlattices yields a new class of functional materials that not only possess or enhance size-related effects but also manifest collective properties.[1−4] Further progress toward the application of such materials is currently limited due to lack of large-scale production and good control of assembled superlattice structures.[5−7] Directed assembly of NPs with projected structure and desired quantity requires thorough understanding of the nucleation mechanisms of the NP supercrystals and the transformative relationships between various superlattice structures.[8−10] NP supercrystals reside naturally at the midpoint of the length scale continuum between atomic crystals and colloidal assemblies. Whereas the self-assembly of the latter is largely entropy-driven, the self-assembly of NP superstructures involves a complex interplay of entropic and enthalpic components. To realize refined and robust control over the formation of superlattices with predefined structures one needs to develop a better understanding of how these interactions impact NP self-assembly.

Spherical NPs represent the simplest colloidal system that has been extensively investigated on their spontaneous self-assembly. At the early stage of nucleation, NPs aggregate randomly and form an amorphous structure with limited short-range ordering.[11,12] Then, NPs minimize the total free energy and crystallize into long-range ordered superlattice structures. These crystals are normally called NP-assembled supercrystals. Experiments disclosed the two types of superlattice polymorphs that dominate the NP assemblies: face-centered-cubic (fcc)[13] and body-centered-cubic (bcc) structure.[1,2,6,8−12] The two types of superlattice polymorphs coexist frequently in nucleated supercrystals and often switch into one another in terms of intermediate lattice distortion, called Bain deformation.[14] It appears that the spherical NPs behave like the hard spheres packing together to form a quite simple superlattice phase diagram, but indeed they undergo an entire procession of nucleation and growth of NP supercrystal with much complexity. Such complicated processes involve not only multiple interactions of NPs with surface-capping ligands and surrounding solvents but suffer also significant impacts from

Received: January 8, 2013
Revised: January 29, 2013
Published: February 8, 2013

additional aspects such as temperature, pressure, evaporation rate, and time scale.[1,2,6,8−12,15−17] Hidden in complexity are always correlations or simple rules, but the question is how to discover these rules and correlations.

In this study, we used oleic acid (OA) capped 3.5 nm PbS NPs as a model system for NP assemblies with experimental control of a variety of parameters. The use of such small NPs and longer chain molecules (~1.8 nm) allows for an increase of X-ray scattering intensity from the low scattering light-element materials such as the hydrocarbon dominant surface ligands, thus enabling feasible detection of the atomic structure changes of not only the NP cores but also the surface-capping OA molecules through access to high-resolution synchrotron small angle (SAXS) and wide-angle X-ray scattering (WAXS) techniques.[18] While SAXS monitors the superlattice polymorphs and inter-NP distances of nucleated supercrystals, WAXS tracks the atomic structural changes of the NP core and the surface-capping molecules.

Here, we report on the discovery of close correlations for the superlattice structures and related phase transformations in nucleated supercrystals as functions of inter-NP distance and packing density of the NP cores. Combining the detected change of surface structure and ordering of surface ligands with the fluctuation of the total free energy over the entire NP−ligand interacting system, we constructed a model that allows for realistic interpretation of the nucleation, superlattice structure, and transformation of the NP-assembled supercrystals.

Experimental Section. *Synthesis of PbS NPs.* The standard procedure given in Nagel et al.[19] was used to prepare the PbS NPs. Briefly, lead acetate (860 mg), oleic acid (3.5 mL), and *n*-trioctylphosphine (5 mL) were dissolved in diphenylether (10 mL). The solution was degassed at 85 °C under vacuum to remove acetate from the lead oleate. The reaction temperature was then increased to 100 °C under nitrogen and 1 mL of sulfur precursor stock solution (80 mg) of thioacetamide (sulfur source) in dimethylformamide (0.5 mL) and *n*-trioctylphosphane (6 mL) was injected. The reaction mixture was stirred for additional five minutes and then cooled down to room temperature. The synthesized NPs were isolated from the reaction mixture by centrifugation and dissolved in chloroform. The NPs were washed by repeating this procedure three times. Eventually, the synthesized NPs were redispersed in chloroform for preservation and further treatment.

Assemblies of PbS NPs. Self-assembled PbS NP superlattices were formed under a variety of experimental conditions. NPs were dispersed in the three types of solvents that include chloroform, toluene, and hexane. The three types of NP-dispersed solutions had the same/closed concentrations for control experiments.

The first set of experiments was controlled for NP assemblies at a fast solvent-evaporation rate. For the three types of NP-dispersed solutions, each one was drop-casted on the three types of substrates including diamond, silica glass, and Kapton tape in air at room conditions. Exclusive of one drop-casted on Kapton tape, the other two samples were heated in an oven with temperature controlled at 50, 100, 142, and 162 °C, respectively. The temperature at each controlled heating step displayed a small fluctuation over a range of 3−5 °C. The heating time differed in step from one to another (1−24 h), but all the samples were heated at each controlled point of temperature and maintained for equivalent time toward consistent comparison. After heating at each controlled temperature, all the samples were characterized using SAXS and WAXS.

The second set of experiments was controlled for NP assemblies at a slow solvent-evaporation rate. Like the first sets of experiments, the three types of NP-dispersed solutions were the same and consisted of chloroform, toluene, and hexane, but differently they were sealed separately in small vials using commercial plastic parafilm to slow solvent evaporation and drying of the nucleated supercrystals. The drying rates between the three samples are slightly different because of different boiling temperatures and mass densities. After slow drying for about three weeks, the small amounts of assembled samples were picked up using a needle for SAXS and WAXS measurements. The residual samples were resealed in vials for continuous aging and preservation. Several months later, all the samples were checked again by SAXS and WAXS. The same procedure was repeated, but the period for the SAXS/WAXS characterization differs from one to another and relies mainly on the time line of the X-ray running cycles scheduled at the Cornell High Energy Synchrotron Source (CHESS).

The two additional sets of experiments were done only for the samples assembled by drying NP-dispersed chloroform solution. One assembled at a fast-evaporation rate was left over in vial without tight sealing for several months to check the air-aging tuned structure change. Another one assembled by slow-evaporation of NP-dispersed chloroform was heated using the same control procedure of temperature as described above. Similarly, both the SAXS and WAXS measurements were performed at CHESS after each heating step.

Transmission Electron Microscopy (TEM) Characterization. The NP-dispersed solution was drop-casted on a carbon-coated copper grid and characterized using high-resolution TEM (HRTEM) with a JEOL JEM 1011 at an acceleration voltage of 100 kV, Philips CM 300 UT at an acceleration voltage of 200 kV, and a JEOL JEM 2200 FS (UHR) with CESCOR and CETCOR corrector at an acceleration voltage of 200 kV.

Synchrotron SAXS and WAXS Measurements. The SAXS and WAXS measurements were performed at the B2 station of CHESS. A double-crystal monochromator was used to convert the white incident X-rays into a monochromatic beam. The X-ray energy was optimized at 25.5, 23, 20, and 18 keV for X-ray scattering measurements. The monochromatic X-ray beam was reduced by a tube collimator down to 100 μm in diameter for illumination of the samples. The X-ray scattering signals from the samples were recorded using a large area MAR345 detector in a transmission mode. Both CeO_2 and Ag-behenate (e.g., $d_{(001)}$ = 58.38 Å) standards were used to calibrate the sample-to-detector distance and the detector tilting parameters for the WAXS and SAXS measurements, respectively. PbS NPs were transferred either onto a transparent tape or into a stainless gasket hole mounted on a sample stage at the B2 station for simultaneous collection of WAXS and SAXS images from the same spot of the samples.[18]

Both SAXS and WAXS information were acquired simultaneously from the same volume of assembled NP samples for reliable comparison and meaningful correlation. Each X-ray exposure yielded both WAXS and SAXS patterns optimized for *d*-spacing range and suitable resolution. After a preliminary estimation and a series of tests, the X-ray energy was optimized at 25.5 keV for the majority of SAXS/WAXS measurements. Once a higher resolution was required

particularly in SAXS range for effectively resolving the superstructures of nucleated supercrystals, the measurements were performed at several reduced X-ray energies of 23, 20, or 18 keV. Using the Fit2D software package, the collected 2D images were integrated into patterns with plot of intensity as a function of 2θ (°) or $Å^{-1}$ for characterization of atomic structures and nanoscale superlattice structures as well as determination of atomic interplanar spacings and inter-NP distances.

Measurements of Oleic Acid and Pb-Oleate. Oleic acid (OA) (Aldrich, 99.9%) was loaded into a diamond anvil cell (DAC) for in situ high-pressure SAXS and WAXS measurements in a pressure cycle of 0−1 GPa. A hole with a diameter of 200 μm was drilled in a stainless gasket after preindentation from 250 μm down to 100 μm in thickness and thus served as the sample chamber. The OA liquid was loaded into the gasket hole with several small ruby chips on the top of the samples and sandwiched between two diamond anvils for in situ pressure measurements. The laser-excited fluorescence peak (R1) from the ruby chips was used to monitor the pressure change. For this typical high-pressure X-ray scattering measurement, the incident X-ray beam was optimized at 25.5 keV to illuminate the samples. A large area MAR345 detector was used to record the SAXS/WAXS signals from the OA samples. Using similar setup but different X-ray energy at 20 keV, the SAXS and WAXS patterns of white Pb-oleate powders were collected at ambient conditions.

Structure Indexing and Lattice Calculations. On the basis of the first observed strong SAXS peak, the full SAXS pattern was calculated for each projected superlattice and thus plotted together with the SAXS pattern collected from nucleated supercrystal for comparison and determination of superlattice structure. After well refinement of the superstructure symmetry, the cell parameters and inter-NP distances were accordingly calculated. More details are described in Supporting Information.

Results and Discussion. TEM characterizations revealed that the synthesized PbS NPs have an average particle diameter of ~3.5 nm (Figure 1a). The hard NP core interacts with surface-capping soft OA molecules to form a hard/soft core−shell structure (Figure 1b). Synchrotron WAXS measurements confirmed that the NP cores exhibit a rocksalt-type cubic structure ($Fm3m$) with a unit cell parameter of a_0 = 5.9502 Å.[20] Spontaneous self-assembly of NPs controlled at a variety of conditions resulted in the nucleation and growth of supercrystals in various superlattice structures, in which NPs serve as the basic building blocks and behave much like atoms occupying the crystallographic sites to form periodically ordered structures. Figure 1c presents several typical SAXS patterns, showing that the NPs spontaneously self-assemble into the three major superlattice polymorphs: (1) short-range ordered fcc-like phase, named as amorphous phase (Figure 1d), (2) bcc (Figure 1e), and (3) fcc phase (Figure 1i). The fcc and bcc phases coexist frequently in nucleated supercrystals (Figure 1f,g). It is quite common that both fcc and bcc phases undergo different magnitude of intermediate lattice distortion and form either a face-centered-tetragonal (fct) (Figure 1h) or a body-centered-tetragonal (bct) structure (Supporting Information Figure S1). Here, fct and bct are simply defined as the tetragonal distortion in which fct is closer to fcc and bct is closer to bcc. The superlattice distortion originates mostly from the existence of an internal stress that deforms the nucleated supercrystals from ideal bcc or fcc lattice into a series of

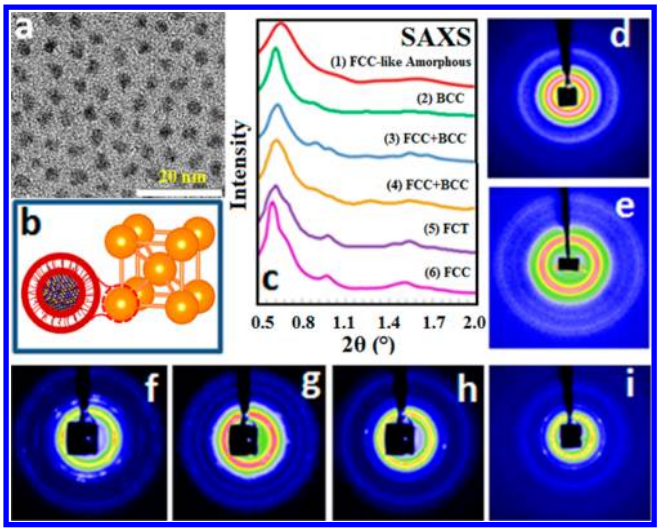

Figure 1. Characterization, decoration, and assembled PbS NP superlattice polymorphs: (a) TEM image of NP monolayer; (b) schematic of a self-assembled bcc superlattice comprised of ligand-decorated NP/OA core−shell NPs as building blocks; (c) typical azimuthally integrated 1D SAXS patterns; (d−i) 2D SAXS images d−f corresponding to 1−6 in panel c, respectively. Note: bcc, body-centered-cubic; fcc, face-centered-cubic; fct, face-centered-tetragonal; amorphous, short-range ordered structure; and fcc + bcc, coexistence of fcc and bcc phase.

intermediate structures (Supporting Information Figure S2). The internal stress frequently exists at interfaces between bcc and fcc phases, such as a series of twinning planes [i.e., {112} planes] that connect the two structures to form single supercrystal-like domain.[16] The internal stress was most likely generated by the drying of NP-assembled supercrystals through evaporation of solvent. Upon evaporation of solvents from either the substrate surface or the vial wall (or bottom), the nucleated NP supercrystals slowly dry up and thus produce a compressive stress along the direction normal to the substrate surface or the vial wall (or bottom), which accordingly results in significant structural distortion of nucleated NP supercrystal.[15,21] In addition, such compressive stresses stored at bcc/fcc interfaces can also explain well the small inter-NP spacings observed from the bcc/fcc coexisted supercrystals.

The experiments discussed above illustrate that complex interplay of driving forces governing the nucleation and growth of PbS NP supercrystals and associated superlattice phase transformation can be derived (Figures 1 and 2). Four major findings of our study include the following: (1) Fast evaporation of NP-dispersed solvents in air favors the formation of an amorphous phase. Unlike the homogenously suspended NPs that were randomly distributed in a dilute solution, this amorphous solid phase instead displays a short-range ordered fcc-like local structure [Figure 1 panels c-(1) and d]. (2) Slow evaporation of NP-dispersed solvents favors an fcc-dominant superlattice that always contains a small fraction of bcc phase. The spotty features shown in the two-dimensional (2D) SAXS images indicate that the nucleated fcc phase hold great coherences of both translation and orientation of NPs over quite expansive domains. Correlating the X-ray illuminated sample size of 100 μm in diameter to the spotty features (i.e., number of the diffraction spots at each ring), the domain size of nucleated supercrystals can be roughly estimated in the order of several tenths of micrometers [Figure 1 panels i and f]. (3)

dx.doi.org/10.1021/nl400084k | *Nano Lett.* 2013, 13, 1303−1311

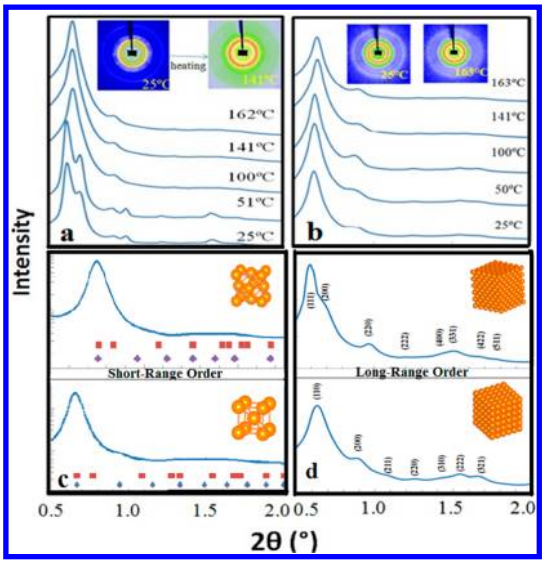

Figure 2. SAXS patterns of observed superlattice phase transformations: (a) thermally driven transformation from fcc and bcc superstructure; (b) thermal stability of the bcc superstructure; (c,d) long-term air-aging tuned fcc−bcc phase transformations at short-range and long-range ordered regions. For the short-range ordered phases (c), red square and blue diamond represent the calculated peak positions of the fcc and bcc superstructures, respectively. Note: Two patterns of insert (c) are not normalized using the same energy.

Thermal treatment accelerates the fcc-to-bcc phase transformation (Figure 2a); the bcc phase remains stable to the peak temperature of 163 °C reached in this study (Figure 2b). Heating the supercrystals in air transforms the fcc completely to bcc superlattice at a temperature of 100 °C (Figure 2a). The smearing feature of 2D SAXS image for the bcc supercrystals recovered from high temperature suggests a significant reduction of single supercrystal domains. (4) Long-term exposure of nucleated supercrystals in air converts the superlattice slowly into bcc-like phase that belongs to one of the two categories, (a) the short-range ordered fcc-like to bcc-like amorphous phase transformation (Figure 2c); and (b) the long-range ordered fcc-to-bcc superlattice phase transformation (Figure 2d). In the long-range ordered region, thermal treatment at temperatures below 50 °C not only facilitates the above phase transformations but also increases the single supercrystal domain size.

The structures of NP superlattices appear at a first glance not to be clearly correlated to processing conditions. But if we sort the superlattice polymorphs by the packing efficiency (the ratio of the NP core to the total volume), they display an apparent change as a function of inter-NP distance. Then, we can immediately correlate the various superlattice polymorphs to the nucleation and growth of NP supercrystals and their superlattice transformations. A plot of the volumetric ratio of the NP core to the total volume in a superlattice unit cell, referred as to the packing density, as a function of inter-NP distance (Figure 3) reveals that the superlattices and associated phase transformations are closely related to the variation of the packing density and the inter-NP distance (see the details for the calculations of the inter-NP distance and the packing density in Supporting Information). This finding further suggests that the formation of supercrystals in different superlattice structures depends on the magnitudes of the core−core, core−ligand, and ligand−ligand interactions that

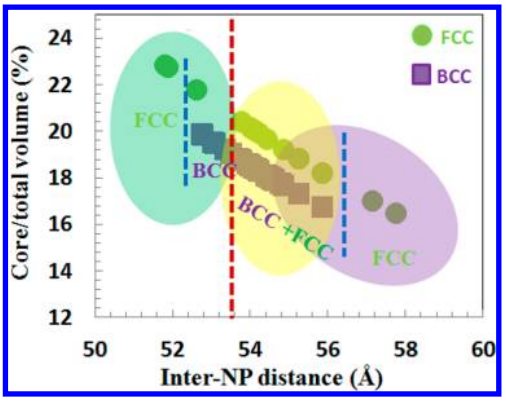

Figure 3. Superlattice developments with correlations to the inter-NP distance and the volumetric ratio of the NP core to the total volume. Left and right regions separated by the dotted red line represent the amorphous/short-range order and crystallized/long-range order regions respectively and the corresponding fcc-to-bcc phase transformations.

change relatively in real NP−ligand interacting system upon environmental variation. At the lower boundary of the observed inter-NP distances, NPs prefer to form an fcc-like amorphous phase that has the highest packing density among the supercrystals nucleated in this study. The nucleation mechanism involves much about the hard core−core interactions. An increase in inter-NP distance tunes supercrystals either in a single bcc phase or in a bcc/fcc mixture in which the interactions between surface ligands start to compete with the interactions between hard NP cores. At the upper boundary of the observed inter-NP distances, NPs tend to form a highly ordered fcc supercrystal that often grows larger. As long as NP cores separate from each other greater, direct interactions between NP cores become weaker, and instead the interactions between surface ligands dramatically enhance, thus governing the nucleation and growth of the supercrystals.

The hard sphere model is mostly used to deal with NPs without considering detailed interactions of the surface-bound ligands.[10,22] The basic hard sphere theory is based on total free energy minimization and the packing density maximization to explain the nucleation of closely packed supercrystals, such as fcc and hexagonal-close-packed (hcp) superlattices[1,2] that have the highest packing density of 74% without consideration of soft surface ligands.[13,23,24] Recent experiments identified one more dominant superlattice, bcc, in NP supercrystals assembled by a broad spectrum of nanoscale materials such as metals and semiconductors,[8−12] and the packing density dramatically reduces to 64%. Combining the surface-capping ligands with hard NP cores and correlating the variation of NP size as a function of ligand length, an alternative model was developed to elucidate the expanded superlattice diagram for NP assemblies.[8] However, newly emergent experiments on PbS and PbSe NPs illustrated the complexities of the rich superlattice phase diagram[15−17,25,26] that challenge the applicability of the basic entropy-driven assembly model.[10,22] To develop a more comprehensive model that describes the formation of observed superlattices and their phase transformations, future studies require not only simple consideration of the packing density and the correlations of NPs to surface ligands but need also additional integration of the atomic structure changes of both NP cores and surface ligands in the nucleation process of various NP assemblies.[27−35] It is most likely that multiple factors interplay together to modify the

dx.doi.org/10.1021/nl400084k | Nano Lett. 2013, 13, 1303−1311

structure and energy level of NP surfaces and eventually change the total free energy of the entire NP−ligand system toward the formation of a stable structured supercrystal. To probe the crystal structure of the NP itself and the surface bound ligands, we studied wide-angle scattering patterns as detailed below.

Figure 4a presents the WAXS patterns of several typical NP supercrystals. They are the same as those for the superlattice

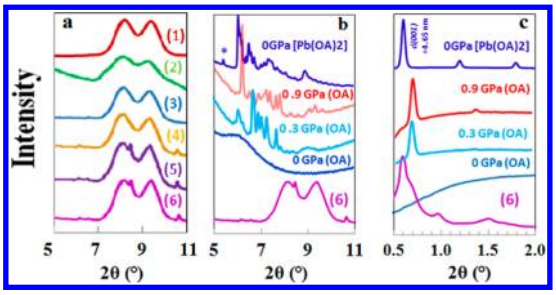

Figure 4. WAXS patterns of NPs in several typical supercrystals with various superstructures (a), WAXS (b), and SAXS (c) patterns of oleic acid (OA) and Pb-oleate under ambient and low pressures. Note: (1) Small but sharp peaks in (a) originate from the ordered OA molecules; (2) No. 6 of insert (b and c) guides comparison of the reflections of OA and Pb-oleate raised from NP assemblies with those from pure solid OA and Pb-oleate phases; 3) * marked inside (b) represents the lamellar peak of (009) [see the full pattern in Supporting Information: Figure S3]; (4) all the plots were normalized using the X-ray wavelength of λ = 0.485946 Å.

determination in Figure 1. Interestingly, the scattering patterns reveal additional reflections that we attribute to ordered structures formed from the oleate ligands themselves. Following the inter-NP distance related superlattice transformations of fcc-like amorphous → mixture of bcc and fcc (or distorted) → fct → highly ordered fcc phase, the surface-capping OA molecules display a noticeable amorphous-to-order structure change, but the bcc-related phases are slightly complicated. This atomic structure change is evident by the emergence of several small but sharp X-ray peaks in the WAXS patterns of several typical supercrystals that display great crystallinity and large inter-NP distance. In-situ WAXS studies of OAs under pressure and Pb-oleate at ambient conditions (Figure 4b) coupled with thorough analyses of NP surface structures suggest that the small peaks are closely related to the locally ordered structures of OA molecules inside nucleated supercrystals.

We have considered two potential crystalline solids that could give rise to the small peaks coexisting with the reflections of PbS NPs embedded in nucleated supercrystals, (1) solid OA phase and (2) Pb-oleate phase. The two phases could be developed by either the ordering of attached OA molecules on PbS NP surfaces or the recrystallization of detached OA molecules. NMR studies of lead salt NPs in solution have illustrated the dynamic nature of the bound and unbound ligands;[36] however, for NP assemblies the equilibrium balance between bound and unbound ligands is less well understood. To characterize the structure of OAs and Pb-oleates we examined SAXS and WAXS signatures. The results (Figure 4b,c) indicate that the small sharp peaks (Figure 4a) match well with the X-ray patterns of the solid OA phase crystallized at low pressure and the Pb-oleate phase at room conditions. It is worthy to point out that both the OA and Pb-oleate phases display extremely strong SAXS peaks from the typical lamellar packing structure that has an interlamellar spacing of $d_{(001)}$ = 4.65 nm (Figure 4c and Supporting Information Figure S3). However, the nucleated supercrystals did not show such a typical lamellar ordered scattering feature. Crystallization of the ligands could occur either in the interstitial of the superlattice or as a separate phase. Our scattering results suggested that the developed ordering of OAs is localized only inside the nucleated supercrystals. This excludes the possibility for that a large portion of OA or Pb-oleate molecules detach from NP surfaces and recrystallize during the evaporation-tuned NP assembling process. Thus, we can conclude that the developed local structures of OAs are indeed hidden in a series of periodically arranged vortexes (e.g., 1.5< size <2.5 nm) embedded in supercrystals in which only OAs hold orientational coherence over large domains of nucleated supercrystals (Scheme 1). Such integrative features that include both the

Scheme 1. (a) Two Types of Local Structures and Regions of Ordered OA Molecules Coated at NP Surfaces in Supercrystals and (b) Extended NP-Ligand Assembled Network

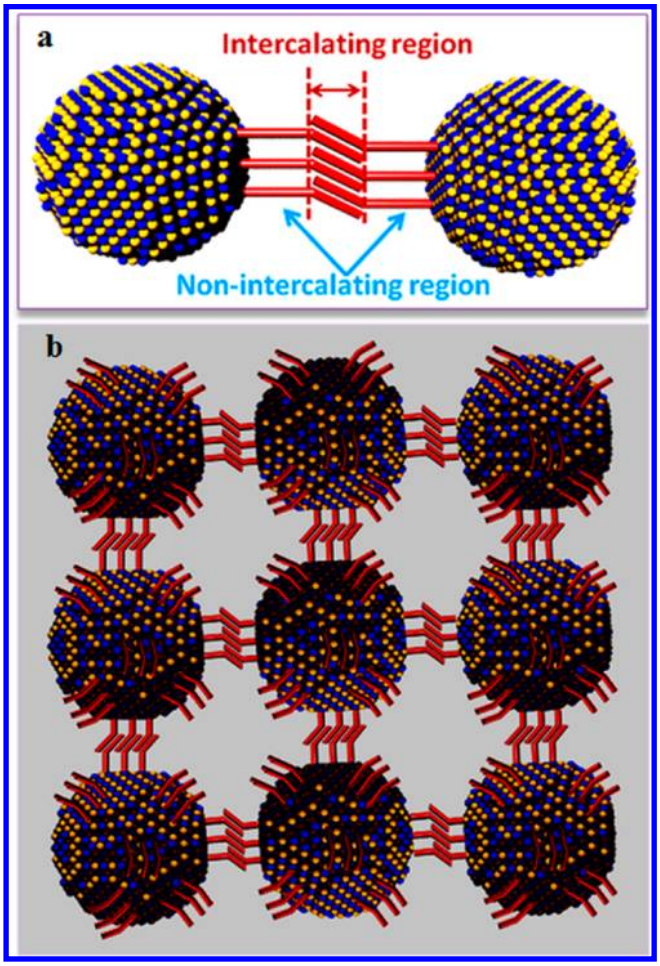

small-volume local order and the largely developed orientation of OAs dismiss the formation of lamellar structure that requires the domain size of embedded vortex at least larger than 4.65 nm (e.g., $d_{(001)}$ = 4.65 nm in Figure 4c)[37−39] and further suggest that a similar structure feature to the single-crystal-like porous materials gives rise to a series of sharp X-ray scattering peaks.[40] Differently, the NPs inside supercrystals display only a broad powder-scattering feature without noticeable texture,

dx.doi.org/10.1021/nl400084k | Nano Lett. 2013, 13, 1303−1311

indicative of lack of apparent orientation for the NPs or at least not as strong as OA molecules (Scheme 1b).

Correlating the structure features of Pb-oleate and OA solids,[37−39] the small sharp peaks can be realistically classified into the following two categories: (1) the peaks overlapping with or nearby the PbS peaks; (2) other peaks without overlapping with PbS peaks (Figure 4b). Upon binding of OA molecules on Pb sites to form Pb-oleates at NP surfaces, if the OAs are coiled and wrapped around NPs, a minimal bridging gap (or area) between NPs is favored to maximize the entropy. The disordered OA molecules diffract like amorphous glasses, yielding a broad diffuse scattering halo. If a greater proportion of crystalline heavy materials such as PbS are mixed, the broad scattering halo from disordered OA molecules should be embedded underneath the total X-ray scattering background and becomes indistinguishable.

Our results point toward an interesting thermodynamic balance of configurational entropy of the NP as hard spheres and, at smaller length scales, enthalpic interactions between the surface bound ligands. Minimizing the area of amorphous OAs between NPs increases the hard-core/soft-shell volumetric ratio tunes up the packing density of NP cores in an unit cell and thus relatively maximizes the configurational (e.g., positional) entropy. In this case, NPs act more or less like the hard spheres and self-assemble into fcc-like amorphous phase that has the highest packing density, such as the observation in this study (Figure 3). Increasing inter-NP distance, the coiled OA molecules at NPs slightly straighten up and intercalate with OAs from neighbor NPs in an order fashion. These slightly ordered OAs in assembled NPs enable producing the two categories of WAXS peaks, which can be reasonably linked with the two types of local ordered OA structures (Scheme 1a). One is located at intercalating region where the CH_2 groups from the OA molecules bonded at two neighboring NPs interact from each other; another at nonintercalating region where OA molecules straighten out from NP surfaces (Scheme 1a).

On the basis of previous X-ray scattering studies on OA solid and Pb-oleate soap,[37−39] the two peaks at 4.5 and 4.3 Å observed from supercrystals suggest the formation of a subcell packing that exists in the intercalating region (Scheme 1a). In this region, the distance between two intercalating OA molecules are approximately half of the intermolecule distances at nonintercalating region, so the H···H interactions between CH_2 groups are favorably developed to link the intercalated OA molecules in an ordered way.[37−39] When this type of local order structure continuously develops, the intercalation-induced OA ordering region enlarges, and accordingly reduces the total free energy of the NP−ligand system. The reduced lattice energy involving each CH_2 group is estimated approximately in the order of 5−8 kJ.[37] The magnitude of the total free energy reduction upon OA ordering depends significantly on (1) how many OA molecules coated at NP surface facet, and (2) how large the portion of each molecule intercalates with another. OA molecule is about 1.8 nm long and consists of one strong C═C bond in middle. If we assume that ligands order along the saturated portion of the chain, then the maximum intercalating length for one pair of OAs is close to 0.9 nm, which is about half the OA molecule length. While the intercalating length is smaller than 0.9 nm (Scheme 1a), the penetration between OA molecules does not suffer a significant physical barrier. Without cost of much external energy for continuous intercalation, a self-assembled process should always prefer an interaction of OAs as long as possible so that the enhanced intermolecular interaction can maximize the structural stability.

Previous studies revealed that OA molecules are bonded on Pb sites at NP surfaces.[28−32] Upon straightening and ordering of OAs at NP surfaces,[39] the intermolecular distances should be more or less equivalent to the interplanar spacing between nearby Pb atoms. To achieve a lower energy state, NPs always involve a series of surface relaxations and reconstructions. This process not only modifies the NP surface structure such as bond length and atomic coordination, but also changes the interplanar distances underneath NP surfaces.[41−43] Therefore, the locally ordered structure of OAs at nonintercalating region produces a series of WAXS peaks that either overlap with or appear nearby the peaks of PbS NPs.[39] In this local structure region (i.e., nonintercalating region in Scheme 1a), the separation distances between OA molecules are wider than those in the intercalating region, resulting in weaker intermolecule interactions. Therefore, the nucleation and growth of NP supercrystal were driven mainly by the enhanced van der Waals forces at intercalating region and increased orientational entropy from the side of OA molecules. Without additional thermal perturbation such as heating, the formation of the two types of local structures results in a decrease of the total free energy through the newly formed H···H bonds. To increase the structure stability, the positive effect from the newly developed ordering of OAs could compromise the negative effect impacted from hard cores through decrease of both configurational entropy and packing density in highly ordered fcc supercrystals that have an enlarged inter-NP distance (Figure 2). The integrative contributions of both the NP cores and the surface ligands to the total energy tend to make balance of each other and thus govern the nucleation and growth of highly ordered supercrystals and their structural stabilities. Given of additional thermal treatment and long-term air aging, the intercalating region enhances intermolecular interactions through formation of H···H bonds, such as the thermally treated and long-term aged supercrystals that developed into a bcc structure and have a slightly shorter inter-NP distance relative to that in highly ordered fcc supercrystals (Figure 2d). In addition, heating and aging are also known to reduce the ligand coverage,[32] so partial loss of ligands could also in turn impact the balance of entropic interactions between NP and enthalpic interactions between the ligands.

To understand more about the nucleation and structure stability of different superlattice polymorphs from the thermodynamic point of view, we further explored the variation of several major lattice planes of NPs as a function of inter-NP distance, allowing for a simple estimation of the surface energy of NPs embedded in supercrystals with various superlattice structures. On the basis of the Wulff-Wigner theory, the surfaces of a spherical NP can be reconstructed by the three low-index planes of {111}, {200}, and {220} that normally have lower surface energy.[19,20,27] For reliable comparison, the interplanar spacings of {111}, {200} and {220} from nucleated supercrystals used in Figure 4 were determined and plotted in Figure 5 against the inter-NP distance. Using bulk PbS as a reference, the amorphous supercrystals display analogous *d*-spacings of {111} and {220}, but a noticeable increase of {200}. The lattice expansion of {200} is indicative of not only a negative surface energy that increases the structure stability but also a tensile stress that broadens the X-ray peaks of PbS NPs and surface ligands (Figure 4a-(2)]. The reduction of surface

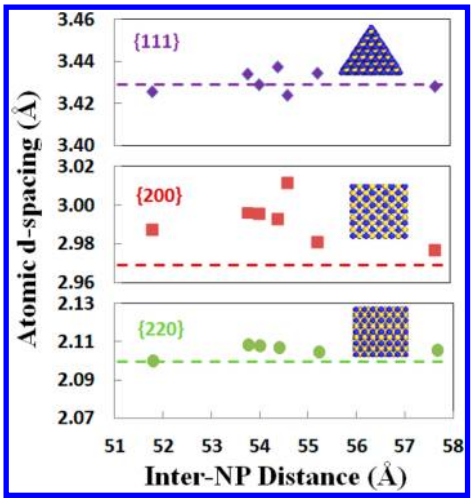

Figure 5. Lattice change of {111}, {200}, and {220} planes of PbS NPs as a function of inter-NP distance. Note: Dotted lines represent the *d*-spacing of bulk PbS as a reference.

energy through {200}-dominated surface reconstruction explains well the observed attachment and subsequent fusion of NPs into {200}-terminated nanosheets at different conditions.[20,44] Upon increase of inter-NP distance, NPs prefer to form a bcc structure that decreases surface energy through expansions of all the three lattice planes, accordingly enhancing the structural stability. As long as the inter-NP distance reaches the upper boundary of the observed range, NPs nucleate in a perfect fcc superlattice that tends to grow into large supercrystal. This highly ordered fcc supercrystal phase reversely displays a lattice shrinkage of {200}, but no apparent lattice variation of {111} and {220}. Such a lattice shrinkage of {200} implies a compressive state and increased surface energy. Thermodynamically, increase of surface energy tends to induce a structural instability. Therefore, it is most likely that an additional contribution from ligand ordering inside supercrystals suppress the surface energy tuned negative effect to maintain the structure stability of nucleated supercrystals. Multiplying the effects contributed from various components with relative change of the total free energy suggests that additional processing favors an ultimate formation of the bcc structure (Figures 2a,b and 5).[15−17,45] In addition, different magnitude of ordering that involves lattice translation and orientation of both the surface-capping molecules and the NP cores across nucleated supercrystal domains[15−17] results in the existence of anisotropic stresses at NP surfaces that provides reasonable explanation for the observed lattice change of {200} facets.[41−43]

Combining experiments and observed structure changes as well as thorough analyses allow one to construct the model as shown in Scheme 2 toward a realistic interpretation of the nucleation and growth of NP assemblies and their superlattice phase transformations. Upon increase of inter-NP distance in nucleated supercrystals, the packing density of hard NP cores in unit cell reduces and accordingly the soft OA molecules modify the makeup at NP surfaces from disorder to order. In the small inter-NP distance region, OA molecules are wrapped in a turmoil state at NP surfaces, maximizing the packing density and configurational entropy for NP-assemblies. Increasing the inter-NP distance tunes the wrapped and constrained surface OA molecules loosen, and slightly increases the conformational (directional) entropy from the side of soft molecules. This contribution compromises the decrease of configurational entropy from another side of hard NP core through reduction of the packing density. Comparative changes from the two different aspects guide the superlattice transformation from short-range ordered fcc to bcc amorphous phase. In the large inter-NP distance region, the fraction of ordered molecules at NP surfaces increases and develops the two types of locally ordered structures. Similar to the nucleation of one atomic crystal from its liquid state, the newly developed ordering of OA molecules reduces the free energy and overcomes the loss of hard core related configurational (positional) entropy. The resulting reduction of total free energy eventually governs the nucleation and growth of highly ordered fcc and bcc phases and subsequent transformations. Thermal treatment and long-term aging of nucleated supercrystal in air reduces the inter-NP distance and the surface energy and increases the intercalating region. Accordingly, increased groups of CH_2 from OA molecules interact together to form H···H bonds (Scheme 1). From one side, the surface molecules reduce the total free energy, and on another side the NP−ligand system reaches a compromise between increased configurational entropy of hard cores and reduced directional entropy of ordered molecules. It

Scheme 2. Constructed Model for Interpreting the Nucleation and Growth of NP Assembled Superlattices[a]

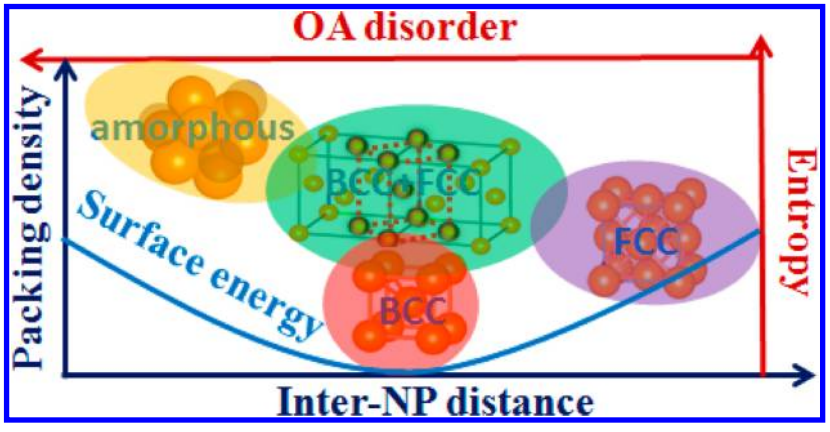

[a]Note: Arrows direct the increase of the magnitude of given parameters, and the entropy given inside represents the contribution only from the NP cores.

dx.doi.org/10.1021/nl400084k | *Nano Lett.* 2013, 13, 1303−1311

is thus suggested that additional thermal treatment or air-aging processes favor the formation of a bcc phase.

The nucleation and growth of NP supercrystals and their phase transformations display great similarities to those in atomic solids. For instance, the most recently developed subnano electron diffraction technique characterized that metallic glasses hold a short-range atomic ordered bcc local structure that is attributed to enhanced performance of their mechanical properties.[46,47] When the building blocks increase in size from atomic to nanoscale, NP-assembled solid tends to behave in a similar way to atomic solid. For example, this study revealed the bcc superlattice as one thermodynamically favorable structure; high-pressure studies demonstrated much more enhanced structure stability for NPs embedded in bcc than in fcc supercrystals.[45] We also observed the smaller inter-NP spacings in the short-range ordered amorphous supercrystal films, which are of typical phenomena in atomic glasses, such as amorphous ices and silica glasses that are more dense than the ordered phases nucleated at similar $P-T$ conditions.[48−50] Considering the low resolutions of existing techniques for materials characterization at atomic scale, NP-assembled supercrystals with fine-tuning of NP particle size can be considered as alternatives to match suitable solution in a series of difficult or extremely challenging studies. Applying the similarities and correlations between materials that have the same structure but different length scale, the results obtained from NP supercrystals can be used to understand the behaviors of atomic solids at various conditions.[51]

Conclusions. Assemblies of 3.5 nm PbS NPs controlled with a variety of experimental conditions and/or procedures result in the nucleation of three independent superlattice polymorphs: fcc-like amorphous, bcc, and fcc phase. The two fcc-related phases stand for the two end members at the two extremes of the observed inter-NP distance range. The bcc and fcc coexist frequently and mostly involve an intermediate tetragonal distortion, resulting in the formation of either a bct or a fct phase. Upon increase of inter-NP distance, supercrystals evolve along a sequence of superlattice transformations from fcc-like amorphous → bcc-like amorphous → mixture of bcc and fcc (or distorted) → fcc phase. This transformative progression was driven by increased ratio of structure ordering and enhanced interactions of surface-capping molecules and associated free energy variation of the entire NP−ligand system. The bcc appears to be one thermodynamically favored superlattice phase that can be tuned through thermal treatment or long-term air-aging. The ultimate formation of the bcc is slightly complicated compared to others and most likely involves a combined effect of enhanced intercalation and partial loss of surface ligands. Additionally, NP-assembled supercrystals can be readily studied by existing analytical techniques, providing a feasible route for understanding the structures and properties of atomic solids at different conditions.

■ ASSOCIATED CONTENT

Ⓢ Supporting Information

Additional data include the calculation methods on packing density and inter-NP distance, additional scheme, and SAXS patterns. This material is available free of charge via the Internet at http://pubs.acs.org.

■ AUTHOR INFORMATION

Corresponding Author

*E-mail: zw42@cornell.edu.

Notes

The authors declare no competing financial interest.

■ ACKNOWLEDGMENTS

We appreciate technical assistance from all the CHESS staff. We are also grateful to Sol Gruner, Roald Hoffmann, and Detlef Smilgies at Cornell for inspiring discussions and many off-campus collaborators for significant suggestions. CHESS is supported by the NSF award DMR-0936384.

■ REFERENCES

(1) Murray, C. B.; Kagan, C. R.; Bawendi, M. G. *Annu. Rev. Mater. Sci.* **2000**, *30*, 545−610.
(2) Murray, C. B.; Kagan, C. R.; Bawendi, M. G. *Science* **1995**, *270*, 1335−1338.
(3) Quan, Z.; Fang, J. Y. *Nano Today* **2010**, *5*, 390−411.
(4) Markovich, G.; Collier, C. P.; Henrichs, S. E.; Remacle, F.; Levine, R. D.; Heath, J. R. *Acc. Chem. Res.* **1999**, *32*, 415−423.
(5) Talapin, D. V.; Lee, J. S.; Kavalenko, M. V.; Shevchenko, E. V. *Chem. Rev.* **2010**, *110*, 389−458.
(6) Pileni, M. P. *Acc. Chem. Res.* **2008**, *41*, 1799−1809.
(7) Semonin, O. E.; Luther, J. M.; Choi, S.; Chen, H.-Y.; Gao, J.; Nozik, A. J.; Beard, M. C. *Science* **2011**, *334*, 1530−1533.
(8) Whetten, R. L.; Shafigullin, M. N.; Khoury, J. T.; Schaaff, T. G.; Vezmar, I.; Alvarez, M. M.; Wilkinson, A. *Acc. Chem. Res.* **1999**, *32*, 397−406.
(9) Goodfellow, B. M.; Korgel, B. A. *ACS Nano* **2011**, *5*, 2419−2424.
(10) Sayle, D. C.; Seal, S.; Wang, Z.; Mangili, B. C.; Price, D. W.; Karakoti, A. S.; Kuchibhatla, S. T. V. N.; Hao, Q.; Mobus, G.; Xu, X.; Sayle, T. X. T. *ACS Nano* **2008**, *2*, 1237−1251.
(11) Sirota, E. B.; Ou-Yang, H. D.; Sinha, S. K.; Chaikin, P. M.; Axe, J. D.; Fujii, Y. *Phys. Rev. Lett.* **1989**, *62*, 1524−1527.
(12) Korgel, B. A.; Fitzmaurice, D. *Phys. Rev. B* **1999**, *59*, 14191−14201.
(13) Both fcc and hcp have the same packing density of 74% and very close free energy, so we describe only the fcc in content.
(14) Bain, E. *Trans. AIME* **1924**, *70*, 25−46.
(15) Bian, K. F.; Choi, J. J.; Kaushik, A.; Clancy, P.; Smilgies, D. M.; Hanrath, T. *ACS Nano* **2011**, *5*, 2815−2823.
(16) Goodfellow, B. M.; Patel, R. N.; Panthani, M. G.; Smilgies, D. M.; Korgel, B. A *J. Phys. Chem. C* **2011**, *115*, 6397−6404.
(17) Nagaoka, Y.; Chen, O.; Wang, Z. W.; Cao, Y. C. *J. Am. Chem. Soc.* **2012**, *134*, 2868−2871.
(18) Wang, Z.; Chen, O.; Cao, C. Y.; Finkelstein, K.; Smilgies, D. M.; Lu, X.; Bassett, W. A. *Rev. Sci. Instrum.* **2010**, *81*, 093902.
(19) Nagel, M.; Hickey, G. S.; Frömsdorf, A.; Kornowski, A.; Weller, H. *Z. Phys. Chemie.* **2007**, *221*, 427−437.
(20) Wang, Z.; Schliehe, C.; Wang, T.; Nagaoka, Y.; Cao, Y. C.; Bassett, W. A.; Wu, H.; Fan, H.; Weller, H. *J. Am. Chem. Soc.* **2011**, *133*, 14848−14487.
(21) Dunphy, D.; Fan, H.; Li, X.; Wang, J.; Brinker, C. J. *Langmuir* **2008**, *24*, 10575−10578.
(22) Korgel, B. A.; Fullam, S.; Connolly, S.; Fitzmaurice, D. *J. Phys. Chem. B* **1998**, *102*, 8379−8388.
(23) Wang, Z. L. *Adv. Mater.* **1998**, *10*, 13−30.
(24) Chen, M.; Pica, T.; Jiang, T. B.; Li, P.; Yano, K.; Liu, J. P.; Datye, A. K.; Fan, H. *J. Am. Chem. Soc.* **2007**, *129*, 6348−6349.
(25) Lee, B.; Podsiadlo, P.; Rupich, S.; Talapin, D. V.; Rajh, T.; Shevchenko, E. V. *J. Am. Chem. Soc.* **2009**, *131*, 1636−16388.
(26) Podsiadlo, P.; Krylova, G.; Lee, B.; Critchley, K.; Gosztola, D. J.; Talapin, D. V.; Ashby, P. D.; Shevchenko, E. V. *J. Am. Chem. Soc.* **2010**, *132*, 8953−8960.
(27) Fang, C.; Van Huis, M. A.; Vanmaekelbergh, D.; Zandbergen, H. W. *ACS Nano* **2010**, *4*, 211−218.
(28) Bealing, C. R.; Baumgardner, W. J.; Choi, J. J.; Hennig, R. G. *ACS Nano* **2012**, *6*, 2118−2127.
(29) Kaushik, A. P.; Claucy, P. *J. Chem. Phys.* **2012**, *136*, 114702.

(30) Moreels, I.; Lambert, K.; De Muynck, D.; Vanhaecke, F.; Poelman, D.; Martins, J. C.; Allan, G.; Hens, Z. *Chem. Mater.* **2007**, *19*, 6101−6106.
(31) Moreels, I.; Lambert, K.; Smeets, D.; De Muynck, D.; Nollet, T.; Martins, J. C.; Vanhaecke, F.; Vantomme, A.; Delerue, C.; Allan, G.; Hens, Z. *ACS Nano* **2009**, *3*, 3023−3030.
(32) Choi, J. J.; Bealing, C. R.; Bian, K.; Hughes, K. J.; Zhang, W.; Smilgies, D.-M.; Hennig, R. G.; Engstrom, J. R.; Hanrath, T. *J. Am. Chem. Soc.* **2011**, *133*, 3131−3138.
(33) Ziherl, P.; Kamien, R. D. *J. Phys. Chem. B* **2001**, *105*, 10147−10158.
(34) Glotzer, S. C.; Anderson, J. A. *Nat. Mater.* **2010**, *9*, 885−887.
(35) Glotzer, S. C.; Engel, M. *Nature* **2011**, *471*, 309−310.
(36) Fritzinger, B.; Moreels, I.; Lommens, P.; Koole, R.; Hens, Z.; Martins, J. C. *J. Am. Chem. Soc.* **2009**, *131*, 3024−3032.
(37) Tandon, P.; Forster, G.; Neubert, R.; Wartewig, S. *J. Mol. Struct.* **2000**, *524*, 201−215.
(38) Lutton, E. S. *J. Am. Oil Chem. Soc.* **1946**, *23*, 265.
(39) Corbeil, M. C.; Robinet, L. *Powder Diffr.* **2002**, *17*, 52−60.
(40) Li, H. Y.; Xin, H. L.; Muller, D. A.; Estroff, L. A. *Science* **2009**, *326*, 1244−1247.
(41) Son, J. S.; et al. *Angew. Chem., Int. Ed.* **2009**, *48*, 6861−6864.
(42) Wang, Z. W.; Wen, X. D.; Hoffmann, R.; Son, J. S.; Li, R.; Fang, C. C.; Smilgies, D. M.; Hyeon, T. *Proc. Natl. Acad. Sci. U.S.A.* **2010**, *107*, 17119−17124.
(43) Hoffmann, R. *Angew. Chem., Int. Ed.* **2012**, DOI: 10.1002/anie.201206678.
(44) Schliehe, C.; Juarez, B. H.; Pelletier, M.; Jander, S.; Greshnykh, D.; Nagel, M.; Meyer, A.; Foerster, S.; Krnowski, A.; Klinke, C.; Weller, H. *Science* **2010**, *329*, 550−553.
(45) Bian, K.; Wang, Z.; Hanrath, T. *J. Am. Chem. Soc.* **2012**, *134*, 10787−10790.
(46) Hirat, H.; Guan, P.; Fujita, T.; Hirotsu, Y.; Inoue, A.; Yavari, A. Y.; Sakurai, T.; Chen, M. W. *Nat. Mater.* **2011**, *10*, 28−33.
(47) Huang, L.; Li, Q. J.; Shan, Z. W.; Li, J.; Sun, J.; Ma, E. *Nature Commun.* **2011**, *2*, 547−551.
(48) Elliot, S. R. *Physics of amorphous materials*; Longman: London, 1988.
(49) Kim, C. U.; Barstow, B.; Tate, M. W.; Gruner, S. M. *Proc. Natl. Acad. Sci. U.S.A.* **2009**, *106*, 4596−4600.
(50) Ojovan, M. I.; Lee, W. E. *J. Phys.: Condens. Matter* **2006**, *18*, 11507−11520.
(51) Navrotsky, A. *Physics and Chemistry of Earth Materials*; Cambridge Press: New York, 1995.